Thermo-mechanically coupled model of diffusionless phase transformation in austenitic steel

Hallberg, Håkan; Håkansson, Paul; Ristinmaa, Matti

Published in:
International Journal of Solids and Structures

DOI:
10.1016/j.ijsolstr.2010.02.019

2010

International Journal of Solids and Structures 2010, 47(11-12), 1580-1591

Thermo-Mechanically Coupled Model of Diffusionless Phase Transformation in Austenitic Steel

Håkan Hallberg, Paul Håkansson and Matti Ristinmaa*

Division of Solid Mechanics
Lund University, Box 118, S-221 00 Lund, Sweden
*matti.ristinmaa@solid.lth.se

Abstract

A constitutive model of thermo-mechanically coupled finite strain plasticity considering martensitic phase transformation is presented. The model is formulated within a thermodynamic framework, giving a physically sound format where the thermodynamic mechanical and chemical forces that drive the phase transformation are conveniently identifiable. The phase fraction is treated through an internal variable approach and the first law of thermodynamics allows a consistent treatment of the internal heat generation due to dissipation of inelastic work. The model is calibrated against experimental data on a Ni-Cr steel of AISI304-type, allowing illustrative simulations to be performed. It becomes clear that the thermal effects considered in the present formulation have a significant impact on the material behavior. This is seen, not least, in the effects found on forming limit diagrams, also considered in the present paper.

Keywords: Phase transformation, thermo-mechanical processes, finite strain plasticity, AISI304, forming limit diagram, FLD

1 Introduction

Phase transformations in metals have a major impact on vital engineering aspects of the material behavior such as ductility, strength and formability. In addition, materials undergoing microstructural changes in terms of diffusionless austenite-martensite transformation have in recent years gained increasing interest in relation to shape memory alloys (SMA:s)

DOI: 10.1016/j.ijsolstr.2010.02.019

and alloys prone to transformation-induced plasticity (TRIP steels). The present work focuses on such diffusionless transformation of an austenitic parent phase into a martensitic. This process was considered already in 1965 by Greenwood and Johnson (1965) who identified a plastic straining in the weaker austenite phase due to the volume increase of the growing, relatively harder, martensite phase. This plastic straining, which may occur even though the externally applied load is in itself insufficient to induce plastic deformation in the material, has subsequently become known as the Greenwood-Johnson effect. Apart from this volumetric deformation, it was also shown by Magee (1969) that an externally applied stress may initiate the formation of selected martensite variants (24 martensite variants are geometrically possible based on the austenitic fcc lattice), resulting in an orientation along preferred directions, a phenomena known as the Magee effect. The martensite formation will thus involve both deviatoric and volumetric deformation components in contrast to the isochoric plastic deformation.

During inelastic deformation of the material, internal heat generation will occur due to dissipation from the plastic slip process and also due to dissipation related to the phase transformation. The martensitic phase transformation is strongly influenced by the thermal conditions. The austenite phase retained at room temperature is metastable and a lowering of the temperature below the M_{s} temperature can result in spontaneous transformation of austenite into martensite as the thermally activated transformation driving force becomes sufficiently large. If the temperature on the other hand is further increased above room temperature, the austenite phase becomes increasingly stable and it is possible to identify a temperature M_{d}, above which no transformation can be induced by plastic deformation. The kinetics of the temperature dependent martensitic transformation was considered in the early model of Olson and Cohen (1975). This model was later modified by e.g. Stringfellow *et al.* (1992) to include the effects of the stress state on the transformation kinetics. These earlier models often use an explicit formulation of the growth of the martensitic phase, based on the number of martensite nucleation sites in the microstructure and the probability of nucleation at those sites. Several models of later date have also been published, of which the works of Leblond *et al.* (1986a,b); Fischer *et al.* (1998); Petit-Grostabussiat *et al.* (2004); Turteltaub and Suiker (2005); Mohr and Jacquemin (2008); Wolff *et al.* (2008); Geijselaers and Perdahcioglu (2009); Lee *et al.* (2009); Mahnken *et al.* (2009) could be mentioned. These models consider phenomenological forms of martensite evolution, coaxial with the applied stress and proportional to the transformation rate. In other model approaches, the microscopic transformation strain is established in a micro region of the material and some homogenization procedure is then employed to obtain the macroscopic transformation strain. Models formulated in this way are presented by e.g. Levitas (1998); Fischer *et al.* (2000); Levitas *et al.* (2002). Thermo-mechanically coupled models, including martensitic phase transformation, are discussed by e.g. Christ and Reese (2009) and Rengarajan *et al.* (1998) in relation to shape memory alloys and by Silva *et al.*

(2004) in relation to quenching.

The present thermo-mechanically coupled constitutive model of martensitic phase transformation is closely related to the isothermal formulation presented in Hallberg *et al.* (2007). In this previous paper, a coherent model of finite strain J_2-plasticity and phase transformation was established using a transformation potential function based on both the second and third invariant of the deviatoric stress tensor. The model was presented together with calibration details, integration of the constitutive relations, formulation of the algorithmic tangent stiffness tensor and numerical simulation examples. The present model is an extension of the previous work, including thermal effects such as the internal heat generation due to the dissipation of internal inelastic work and heat released during phase transformation. As it appears, this consistent treatment of the thermal effects and the temperature influence on the evolution of a martensitic phase in the austenitic parent phase, gives important additions to the previous model with significant impact on the material behavior.

Starting with a section on the finite strain kinematics, the present constitutive model is then formulated within a thermodynamic framework using the first and second law. This allows identification of the thermodynamic mechanical and chemical forces, driving the phase transformation towards a lowering of the Gibbs energy in the material microstructure. Using a continuum-mechanical formulation, the present model is suitable for large-scale simulations of processes where the austenitic material is influenced by martensite formation. This is shown by illustrative numerical simulation examples, following a calibration of the model against experimental data on a Ni-Cr steel of AISI304-type. In addition, since austenitic stainless steels are important in sheet metal forming operations such as deep-drawing, the effects of martensite evolution on forming limit diagrams of such a material is studied. Some concluding remarks then finishes the paper.

2 Kinematics

The motion of a particle is described by a nonlinear function $\boldsymbol{\varphi} = \boldsymbol{\varphi}(\boldsymbol{X}, t)$, which maps the position of particles in the reference configuration $\boldsymbol{X}$ at time t to their corresponding position in the current configuration $\boldsymbol{x}$. The deformation gradient, defined as $\boldsymbol{F} = \partial_{\boldsymbol{X}} \boldsymbol{\varphi}$ maps line segments in the neighborhood of $\boldsymbol{X}$ from the reference configuration to the current configuration. The deformation gradient will also provide a relation between the densities in the different configurations, $J = \rho_0/\rho = \det(\boldsymbol{F})$, where ρ and ρ_0 are the densities in the current and reference configuration, respectively, and where $\det(\cdot)$ denotes the determinant. To separate reversible deformation from irreversible, a multiplicative split of the deformation gradient is adopted, cf. Kröner (1959) and Lee and Liu (1967), according to

$$\boldsymbol{F} = \boldsymbol{F}^{\mathrm{r}} \boldsymbol{F}^{\mathrm{ir}} \tag{1}$$

where the reversible part, $\boldsymbol{F}^{\mathrm{r}}$, includes elastic deformation as well as thermal volumetric deformation. The irreversible part, $\boldsymbol{F}^{\mathrm{ir}}$, includes plastic deformation due to slip and deformations due to phase transformation. The velocity gradient, $\boldsymbol{l} = \dot{\boldsymbol{F}}\boldsymbol{F}^{-1}$, is split into one part belonging to the recoverable deformation and one part belonging to the irreversible deformation, i.e

$$\boldsymbol{l} = \boldsymbol{l}^{\mathrm{r}} + \boldsymbol{l}^{\mathrm{ir}} \quad \text{where} \quad \boldsymbol{l}^{\mathrm{r}} = \dot{\boldsymbol{F}}^{\mathrm{r}}\boldsymbol{F}^{\mathrm{r}-1} \quad \text{and} \quad \boldsymbol{l}^{\mathrm{ir}} = \boldsymbol{F}^{\mathrm{r}}\dot{\boldsymbol{F}}^{\mathrm{ir}}\boldsymbol{F}^{\mathrm{ir}-1}\boldsymbol{F}^{\mathrm{r}-1} \tag{2}$$

For coupled thermo-mechanical problems, the use of a thermodynamical framework provides a base for the balances laws, i.e. the equations of motion and the heat equation. One of the benefits of this approach is that the coupling between the balance laws and the constitutive equations, for instance in terms of the heat generation, appears naturally. The Helmholtz energy is used to describe the energy stored in the material microstructure and it is dependent on state variables such as the absolute temperature θ. These state variables are quantities that define the elastic part of the deformation and also variables related to the deformation hardening and the phase fraction. The quantities which define the mechanical state of the body, including the phase fraction, are collected in a set $\boldsymbol{A}$. Without yet specifying the specific expression for the Helmholtz energy, this function is assumed to appear as $\psi = \psi(\boldsymbol{A}, \theta)$. The first law of thermodynamics, which ensures energy balance, can with the Helmholtz energy function be reformulated as the heat equation. Following Håkansson *et al.* (2005) the heat equation takes the following form

$$\rho_0 c\dot{\theta} = \mathcal{D}_{\mathrm{mech}} + \rho_0 r + \rho_0 \frac{\partial^2 \psi}{\partial\theta\partial\boldsymbol{A}} : \dot{\boldsymbol{A}} - J\mathrm{div}(\boldsymbol{q}) \tag{3}$$

where $\mathcal{D}_{\mathrm{mech}}$ is the mechanical part of the dissipation, which is given by the constitutive model, and where $(\cdot) : (\cdot)$ denotes tensorial contraction over two indices. A fixed Cartesian base is used for all tensorial quantities throughout the present work. Also found in (3), r is a heat source and $\boldsymbol{q}$ is the heat flux. In addition, $\mathrm{div}\,(\cdot)$ denotes the divergence operator. The specific heat, c, is also introduced as $c = -\theta\frac{\partial^2\psi}{\partial\theta^2}$. The mechanical dissipation originates from the dissipation inequality which follows from the second law of thermodynamics. The dissipation inequality can be expressed as

$$\mathcal{D} = \boldsymbol{\tau} : \boldsymbol{d} - \rho_0 \frac{\partial \psi}{\partial \boldsymbol{A}} : \dot{\boldsymbol{A}} - \frac{J}{\theta}\frac{\partial \theta}{\partial \boldsymbol{x}} \geq 0 \tag{4}$$

where $\boldsymbol{\tau}$ is the Kirchhoff stress tensor and $\boldsymbol{d}$ the rate of deformation tensor, i.e. $\boldsymbol{d} = \mathrm{sym}(\boldsymbol{l})$. Note that the notation $\mathrm{sym}\,(\cdot)$ was introduced here to indicate the symmetrical part of a tensorial quantity. The dissipation can be conceptually split into two parts where the mechanical component

$$\mathcal{D}_{\mathrm{mech}} = \boldsymbol{\tau} : \boldsymbol{d} - \rho_0 \frac{\partial \psi}{\partial \boldsymbol{A}} : \dot{\boldsymbol{A}} \tag{5}$$

act as a heat source in the heat equation (3) and is determined from the choice of the constitutive model, cf. Ristinmaa *et al.* (2007). The second component is the thermal dissipation $\mathcal{D}_{\text{therm}} = -\frac{J}{\theta}\frac{\partial\theta}{\partial\boldsymbol{x}}$ which is always positive due to the use of Fourier's law, $\boldsymbol{q} = -k\frac{\partial\theta}{\partial\boldsymbol{x}}$, as the constitutive law for the heat flux. Here, the parameter k denotes the heat conduction. The heat equation in (3) together with the equations of motion

$$\text{div}(\boldsymbol{\sigma}) - \boldsymbol{b} = \boldsymbol{0} \tag{6}$$

serves as the base for the coupled finite element equations in the thermo-mechanical problem. In (6), the Cauchy stress tensor is denoted by $\boldsymbol{\sigma} = \boldsymbol{\tau}/J$ and $\boldsymbol{b}$ represents the body force vector.

3 Constitutive model

The present constitutive model is formulated to capture material mechanisms such as the plastic flow due to slip by dislocation movements, changes in the crystallographic structure due to diffusionless phase transformation driven by mechanical and thermal loading, as well as heat generation due to the just mentioned mechanisms. The temperature dependence of the material properties are also considered in the model. The material consists of two different phases, austenite and martensite, with the volume fraction of martensite being denoted by z, i.e. when $z = 1$ the material consists purely of martensite and when $z = 0$ only austenite is present. The general form of the Helmholtz energy function is a mixture between the two phases, i.e. $\psi = (1-z)\psi_{\text{a}} + z\psi_{\text{m}}$, where the subscripts a and m denote the austenite phase and the martensite phase, respectively. The elastic behavior of the two phases can be regarded as equal and it is also assumed that the hardening in the phases is the same. This reasoning results in the following form of the Helmholtz energy function

$$\rho_0\psi = \rho_0\psi^{\text{r}} + \rho_0\psi^{\text{ir}} + (1-z)\rho_0\psi_{\text{a}}^{\text{chem}} + z\rho_0\psi_{\text{m}}^{\text{chem}} \tag{7}$$

where the function is split into one part, ψ^{r}, which corresponds to the elastic and thermal expansion behavior, and one part, ψ^{ir}, which includes the plastic hardening. The last two terms, $\psi_{\text{a}}^{\text{chem}}$ and $\psi_{\text{m}}^{\text{chem}}$, are the chemical energies of the respective phases, cf. Fischer *et al.* (1994). This internally stored energy is different for the two phases and it will influence the heat generation during phase transformation as well as the transformation itself. In the previous section it was assumed that the Helmholtz energy was a function of the temperature and the variable set $\boldsymbol{A}$. As in Hallberg *et al.* (2007), the Helmholtz energy function is here chosen to be a function on the form $\psi = \psi(\boldsymbol{b}_{\text{i}}^{\text{r}}, J^{\text{r}}, \kappa, \theta, z)$, where $\boldsymbol{b}_{\text{i}}^{\text{r}} = (J^{\text{r}})^{-2/3}\boldsymbol{F}^{\text{r}}\boldsymbol{F}^{\text{rT}}$ is the isochoric – denoted by a subscript i – reversible left Cauchy-Green deformation tensor and $J^{\text{r}} = \det(\boldsymbol{F}^{\text{r}})$ the reversible Jacobian. In addition, κ is an internal variable related to the isotropic hardening. The reversible part of the Helmholtz energy is

chosen in order to obtain a Neo-Hookean elastic behavior controlled by a generalized shear modulus G and a corresponding bulk modulus K, i.e.

$$\rho_0\psi^{\mathrm{r}} = \frac{1}{2}K\left[\frac{1}{2}\left(J^{\mathrm{r}2}-1\right)-\ln\left(J^{\mathrm{r}}\right)\right]+\frac{1}{2}G\left[\mathrm{tr}\left(\boldsymbol{b}_{\mathrm{i}}^{\mathrm{r}}\right)-3\right]-\frac{3}{2}\alpha K\left(J^{\mathrm{r}}+\frac{1}{J^{\mathrm{r}}}\right)\Delta\theta \tag{8}$$

where $\mathrm{tr}\left(\cdot\right)$ was introduced to denote the trace of a tensorial quantity. The last term in (8) specifies the thermal expansion controlled by the thermal expansion coefficient α and the difference between the current temperature and an initial temperature θ_{init}, i.e. $\Delta\theta = \theta - \theta_{\mathrm{init}}$. The plastic hardening is included in the irreversible part of the energy function through

$$\rho_0\psi^{\mathrm{ir}} = \frac{1}{2}H\kappa^2 \tag{9}$$

In the chemical part of the Helmholtz energy, the specific heat c_{p} and the entropy s_0 are included, parameters which are different for austenite and martensite as indicated by the superscripts a and m. The specific form of the chemical energy components, a form also used by e.g. Fu *et al.* (1993), are taken as

$$\rho_0\psi_{\mathrm{a}}^{\mathrm{chem}}\left(\theta\right) = -\rho_0 s_0^{\mathrm{a}}\left(\theta-\theta_0\right)+\rho_0 c_{\mathrm{p}}^{\mathrm{a}}\left[\left(\theta-\theta_0\right)-\theta\ln\frac{\theta}{\theta_0}\right] \tag{10}$$

and

$$\rho_0\psi_{\mathrm{m}}^{\mathrm{chem}}\left(\theta\right) = -\rho_0 s_0^{\mathrm{m}}\left(\theta-\theta_0\right)+\rho_0 c_{\mathrm{p}}^{\mathrm{m}}\left[\left(\theta-\theta_0\right)-\theta\ln\frac{\theta}{\theta_0}\right] \tag{11}$$

where θ_0 is a reference temperature. By using the arguments of Coleman and Gurtin (1967) the mechanical dissipation can now, employing the specified format of the Helmholtz energy function, be expressed as

$$\mathcal{D}_{\mathrm{mech}} = \boldsymbol{\tau} : \mathrm{sym}(\boldsymbol{l}^{\mathrm{ir}}) - R\dot{\kappa} - Q\dot{z} \tag{12}$$

where it is used that

$$\boldsymbol{\tau} = 2\rho_0\frac{\partial\psi}{\partial\boldsymbol{b}^{\mathrm{r}}}\boldsymbol{b}^{\mathrm{r}}, \quad R = \rho_0\frac{\partial\psi}{\partial\kappa} \quad \text{and} \quad Q = \rho_0\frac{\partial\psi}{\partial z} \tag{13}$$

The Kirchhoff stress tensor can with (8) and (13) be retrieved as

$$\boldsymbol{\tau} = G\boldsymbol{b}_{\mathrm{i}}^{\mathrm{r,dev}}+\frac{1}{2}K\left(J^{\mathrm{r}2}-1\right)\mathbf{1}-\frac{3}{2}\alpha K\left(J^{\mathrm{r}}+\frac{1}{J^{\mathrm{r}}}\right)\Delta\theta\mathbf{1} \tag{14}$$

where $(\cdot)^{\mathrm{dev}}$ denotes the deviatoric part of a tensorial quantity and where $\mathbf{1}$ is the second order identity tensor. It is assumed that the evolution of the irreversible deformation due to

plastic slip and the one due to phase transformation can take place independently of each other. It is then possible to split the irreversible velocity gradient into two components, giving $\boldsymbol{l}^{\mathrm{ir}} = \boldsymbol{l}^{\mathrm{p}} + \boldsymbol{l}^{\mathrm{tr}}$, where the superscript p denotes the component related to plastic slip and accordingly a superscript tr denotes the component related to phase transformation. At this stage it is also reasonable to assume that $\boldsymbol{l}^{\mathrm{tr}}$ appears with a format given by the rate of the phase transformation multiplied by a tensor function that can be dependent on various quantities such as the stress state, the temperature and so on. Thus, $\boldsymbol{l}^{\mathrm{ir}}$ can be expressed as

$$\boldsymbol{l}^{\mathrm{ir}} = \boldsymbol{l}^{\mathrm{p}} + \boldsymbol{h}(\boldsymbol{\tau}, \kappa, z, \theta)\dot{z} \tag{15}$$

Several authors, e.g. Levitas *et al.* (1998); Ganghoffer and Simonsson (1998); Fischer *et al.* (2000), formulate the deformation related to phase transformation based on a micromechanical reasoning. In the present macroscopic model, however, a different approach is taken. Instead of establishing the deformation gradient related to phase transformation, the evolution law for the transformation velocity gradient $\boldsymbol{l}^{\mathrm{ir}}$ is derived, as shown below. The multiplicative decomposition of the deformation gradient in the present macroscopic model, cf. (1), includes a homogenized change of the crystal lattices due to phase transformation and due to plastic slip. It is, however, the elastic part of the deformation gradient that give rise to the stresses in the material. The use of a transformation potential function and related aspects of model kinematics are discussed in detail in the preceding paper by the authors, cf. Hallberg *et al.* (2007).

The split of $\boldsymbol{l}^{\mathrm{ir}}$ according to (15) results in a mechanical dissipation that can be separated into one part belonging to the slip deformation and one part belonging to the phase transformation, i.e. (12) can be reformulated as

$$\mathcal{D}_{\mathrm{mech}} = \boldsymbol{\tau} : \mathrm{sym}(\boldsymbol{l}^{\mathrm{p}}) - R\dot{\kappa} + (\boldsymbol{\tau} : \boldsymbol{h} - Q)\dot{z} \tag{16}$$

A yield surface of von Mises type is used to determine the onset of plastic deformation due to slip. In comparison with a "standard" elasto-plastic model, the yield surface does not define the elastic region since the irreversible deformation due to phase transformation can occur independently of the plastic deformation. The von Mises yield surface, with isotropic hardening, is here expressed as

$$f = \sigma_{\mathrm{eff}} - \sigma_{\mathrm{y}}(R, z, \theta) = 0 \tag{17}$$

where the effective stress is defined as $\sigma_{\mathrm{eff}} = (\frac{3}{2}\boldsymbol{\tau}^{\mathrm{dev}} : \boldsymbol{\tau}^{\mathrm{dev}})^{1/2}$. The current yield stress is assumed to have the format

$$\sigma_{\mathrm{y}}(R, z, \theta) = \sigma_{\mathrm{y0}}(z, \theta) + R(\kappa) \tag{18}$$

The initial yield stress, σ_{y0}, for austenite and martensite, respectively, are vastly different, the yield stress of the martensite phase being several times higher than that for the austenite

phase. Thus, the constitutive model on the continuum level must predict a homogenized behavior of a material containing an arbitrary fraction of martensite. Mixture laws for the yield stresses of the phases are discussed by e.g. Leblond *et al.* (1986b) and Petit-Grostabussiat *et al.* (2004). In the present model it is assumed that the homogenized yield stress of the material can be described by a relation of the form

$$\sigma_{\mathrm{y0}}\left(z,\theta\right) = m\left(z\right) p\left(\theta\right) \tag{19}$$

where $p(\theta)$ is a temperature-dependent function and where $m(z)$ is a function of the volume fraction of martensite with $m(0) = 1$. The situation $m = 1$ corresponds to $p(\theta) = \sigma_{\mathrm{y0}}^{\mathrm{a}}(\theta)$, the initial yield stress of the austenitic phase. The forms of the functions m and p are specified later on, in relation to the calibration of the model.

The non-associated evolution laws for κ and $\boldsymbol{l}^{\mathrm{p}}$ are based on the following potential function

$$g(\boldsymbol{\tau}, R, z, \theta) = f(\boldsymbol{\tau}, R, z, \theta) + \frac{1}{2}\frac{R^2}{R_\infty} \tag{20}$$

where R_∞ is a material parameter related to the saturation level of the deformation hardening. The potential function (20) leads to the evolution laws being defined as

$$\mathrm{sym}\left(\boldsymbol{l}^{\mathrm{p}}\right) = \lambda \frac{\partial g}{\partial \boldsymbol{\tau}^{\mathrm{dev}}} \tag{21}$$

and

$$\dot{\kappa} = -\lambda \frac{\partial g}{\partial R} \tag{22}$$

where λ is a plastic multiplier. These evolution laws, together with the form of the component ψ^{ir} of the Helmholtz energy function stated in (9), result in an exponential form of hardening.

Transformation of the austenitic phase into martensite can occur independently of the plastic deformation. The transformation is modeled as an irreversible process and reversed transformation, for instance due to heat treatments, is not considered. The transformation is driven by a thermodynamic force, F, conjugated to $\dot{z}$, which can be found in the mechanical dissipation (16). This thermodynamic force is defined as

$$F = F_{\mathrm{mech}} + F_{\mathrm{chem}} \tag{23}$$

where the mechanical component of the driving force is denoted by $F_{\mathrm{mech}} = \boldsymbol{\tau} : \boldsymbol{h}$ and where the corresponding chemical driving force is denoted by $F_{\mathrm{chem}} = -Q$, cf. also (13). On a micromechanical level, austenitic micro-regions change their lattice structure into that of martensite when the thermodynamic force acting on the region exceeds a certain threshold

value, cf. Fischer (1990). On a macroscale, the homogenized condition for transformation results in a transformation surface similar to a plastic yield surface, i.e.

$$h = F - F_{\text{trans}}(z, \theta) = 0 \tag{24}$$

where the threshold F_{trans} due to the homogenization is similar to a hardening, however dependent on z. The specific form of F_{trans} is chosen in connection with the calibration of the model. The explicit form of transformation condition is to a large extent described by $\boldsymbol{h}$, found in (15). In the present model, $\boldsymbol{h}$ is chosen in the same way as in Hallberg *et al.* (2007), where an associated form of the evolution law for $\boldsymbol{l}^{\text{tr}}$ is used, giving

$$\boldsymbol{l}^{\text{tr}} = \dot{z}\boldsymbol{h} = \dot{z}\frac{\partial h}{\partial \boldsymbol{\tau}} \tag{25}$$

The format of the transformation condition h also follows the formulation given in Hallberg *et al.* (2007), i.e.

$$h = \widetilde{K}\left(\bar{\sigma}_{\text{eff}} + \frac{1}{3}\delta I_1\right) - Q - F_{\text{trans}}(z, \theta) = 0 \tag{26}$$

where

$$\bar{\sigma}_{\text{eff}} = \left(3J_2 + 3b\frac{J_3}{J_2^{1/2}}\right)^{1/2} \tag{27}$$

The J_3-invariant in (27) is defined as $J_3 = \frac{1}{3}\text{tr}(\boldsymbol{\tau}^{\text{dev}}\boldsymbol{\tau}^{\text{dev}}\boldsymbol{\tau}^{\text{dev}})$. Additional material parameters are introduced in (26) and (27) through $\widetilde{K}$, δ and b. The values of these parameters are determined during the calibration of the model. The parameter b controls the shape of the transformation surface in the deviatoric plane. If b is chosen as 0, the circular von Mises surface is obtained, but to better reflect the Magee effect a non-circular surface is used.

In Olson and Cohen (1972), two conceptually different phase transformation processes are identified as "stress-assisted" and "strain-induced" transformation, respectively. The present model incorporates both of these processes since phase transformation and plasticity may occur independently of each other in the model, each being defined in stress-space by a transformation surface and a yield surface, respectively. This allows strain-induced and stress-assisted phase transformation to be phenomenologically captured. It is noted that at stresses below the yield stress of austenite, phase transformation can take place in the model and result in "stress-assisted" transformation. Correspondingly, at stresses above the yield limit of austenite, phase transformation takes place together with plastic straining, giving "strain-induced" transformation. In addition, the temperature dependence of the model results in a formulation that allows phase transformation at low temperatures

without plastic deformation and also, at higher temperatures, increasing stress is required to drive the transformation and hence increasing plastic deformation is present during the phase transformation. The fact that phase transformation and plastic slip can occur independently of each other can be further illustrated by defining a domain $\mathcal{P}(z,\theta)$ related to plasticity according to

$$\mathcal{P}(z,\theta) = \{(\boldsymbol{\tau}, R) \mid f(\boldsymbol{\tau}, R, z, \theta) \leq 0\} \tag{28}$$

where f is the yield function. The boundary of $\mathcal{P}(z,\theta)$, i.e. $f = 0$, constitutes the yield surface. Note that, in contrast to classical plasticity, $\mathcal{P}(z,\theta)$ does not define a purely elastic region in the present model, since phase transition is permitted to take place within $\mathcal{P}(z,\theta)$. In a corresponding manner, a domain $\mathcal{T}(\theta)$ related to phase transformation can also be defined as

$$\mathcal{T}(\theta) = \{(F, z) \mid h(F, z, \theta) \leq 0\} \tag{29}$$

where h is the transformation potential function. With the two domains defined by (28) and (29), respectively, a purely elastic domain can also be defined as

$$\mathcal{E} = \mathcal{P} \cap \mathcal{T} \tag{30}$$

It is concluded that phase transition can take place within $\mathcal{P}$ also when no plastic strains develop. It can also be concluded that a plastic response can occur within the domain $\mathcal{T}$ also when no transformation strains are developed.

4 Numerical examples

The calibration of the model is done in order to capture the characteristics of an austenitic Ni-Cr steel (AISI304). The choice of material parameters are based on the work described in Hallberg *et al.* (2007). A few alterations have been made here, however, in order to include the temperature dependence into the model. The elastic properties of the model are given by $K = 167$ GPa, $G = 77$ GPa and the thermal expansion coefficient is set to $\alpha = 1 \times 10^{-5}$ 1/K. The initial yield stress of the austenite phase, cf. (19), is for simplicity assumed to vary linearly with temperature according to

$$\sigma_{\mathrm{y0}}^{\mathrm{a}}(\theta) = 690 - 1.25\theta \text{ MPa} \tag{31}$$

an approximation valid in the temperature interval between 213 and 313 K, and considered here. In Hallberg *et al.* (2007), it was found that the z-dependence of the initial yield stress of the dual phase material, cf. (19), could be captured by a relation on the form

$$m(z) = 1 + 0.81\,[\exp(1.64z) - 1] \tag{32}$$

Mixture laws on this format have been previously used also by e.g. Ludwigson and Berger (1969); Ramirez *et al.* (1992). In addition, the parameters related to the hardening are set to $R_\infty = 1250$ MPa and $H = 2350$ MPa.

The shape of the transformation surface in the deviatoric plane is in (27) determined by the parameter $b = 0.35$ while the hydrostatic behavior is controlled by the parameter $\delta = 0.29$. These parameters are found from the micro-mechanical analysis described in Hallberg *et al.* (2007).

The procedure for calibrating the transformation threshold function F_{trans} in (24) follows Hallberg *et al.* (2007). In the present case the resulting F_{trans} function is slightly modified due to the temperature dependence and is chosen as

$$\frac{F_{\text{trans}}(z,\theta)}{\widetilde{K}} = c_1 + c_2\left(\theta\right)\left[1-\exp(-c_3 z)\right]\left[1-c_4\ln(1-z)\right] \tag{33}$$

with the following parameters

$$c_1 = 1246 \text{ MPa}, \quad c_2\left(\theta\right) = 198 + \left(\frac{\theta}{214}\right)^{13.3} \text{ MPa}, \quad c_3 = 29.5, \quad c_4 = 2.7$$

which were obtained through numerical optimization, giving the appearance of the transformation threshold function as shown in Fig. 1. It should be noted that the present calibration of F_{trans} is only valid within the considered temperature range of 213-313 K. Considering (33) and Fig. 1a, it can be noted that the z-dependence of F_{trans} involves two terms. The exponential term describes the behavior at low values of z while the second, logarithmic, term dictates the behavior at higher values of z. This formulation also ensures that the volume fraction of martensite is kept in the interval of 0 to 1. The temperature dependence of the transformation threshold is given by the coefficient c_2 in (33). In Fig. 1b, this temperature dependence is illustrated for fixed levels of martensite content. At lower temperatures the function is relatively constant, while F_{trans} will increase with increasing temperature to restrict the progression of phase transformation under such thermal conditions. The parameter $\widetilde{K}$, entering the transformation potential function (26), is set to 0.185. For the specification of the parameters in (10) and (11), the choice made by Berveiller and Fischer (1997) is used. In the formulation of the model only the difference between s_0^{a} and s_0^{m} is used, giving $s_0^{\text{a}} - s_0^{\text{m}} = 0.106$ J/kgK with a reference temperature of $\theta_0 = 440$ K. Expression (7) together with (10) and (11) result in a global specific heat given by $c = (1-z)c_{\text{p}}^{\text{a}} + z c_{\text{p}}^{\text{m}}$. The parameters are set to $c_{\text{p}}^{\text{a}} = 450$ J/kgK and $c_{\text{p}}^{\text{m}} = 415$ J/kgK.

Other parameters also required in the coupled thermo-mechanical analysis are the mass density $\rho_0 = 7800$ kg/m^3 and the heat conductivity $k = 45$ W/mK.

4.1 Uniaxial tension

To illustrate the calibration of the model, uniaxial tensile test have been simulated at a strain rate of 1 s^{-1}. The results can be seen in Fig. 2. Isothermal conditions were

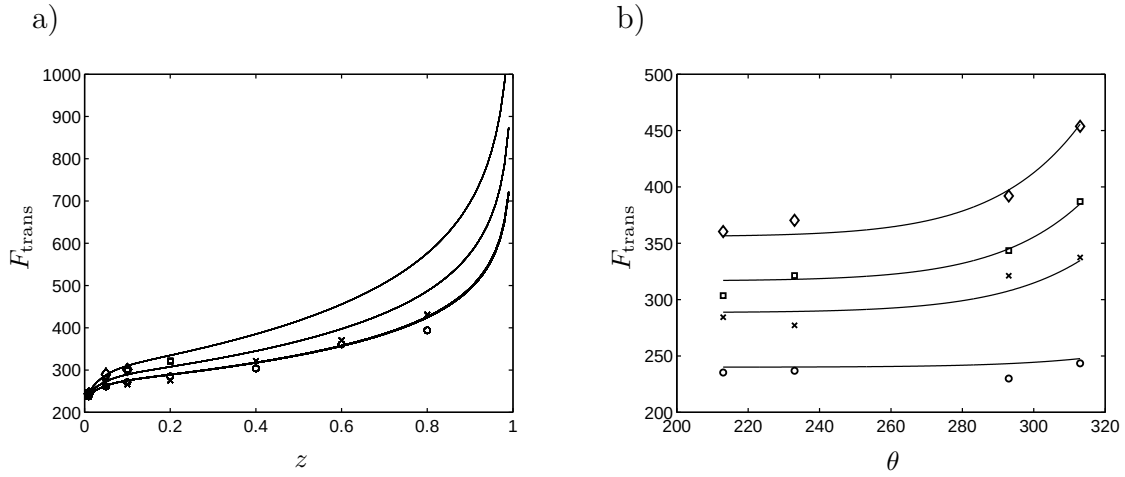

Figure 1: (a) Transformation threshold function F_{trans} as a function of the volume fraction of martensite for constant temperatures, shown by: ○ – 213 K, × – 233 K, □ – 293 K and ◇ – 313 K. (b) Transformation threshold function F_{trans} as a function of the absolute temperature. The constant martensite fractions are ○ – 0.6, × – 0.4, □ – 0.2 and ◇ – 0.01. The experimental data is taken from Onyuna (2003).

defined in the simulations to allow comparison with the material response reported from experimental measurements on an austenitic steel of AISI304-type, cf. Onyuna (2003). The

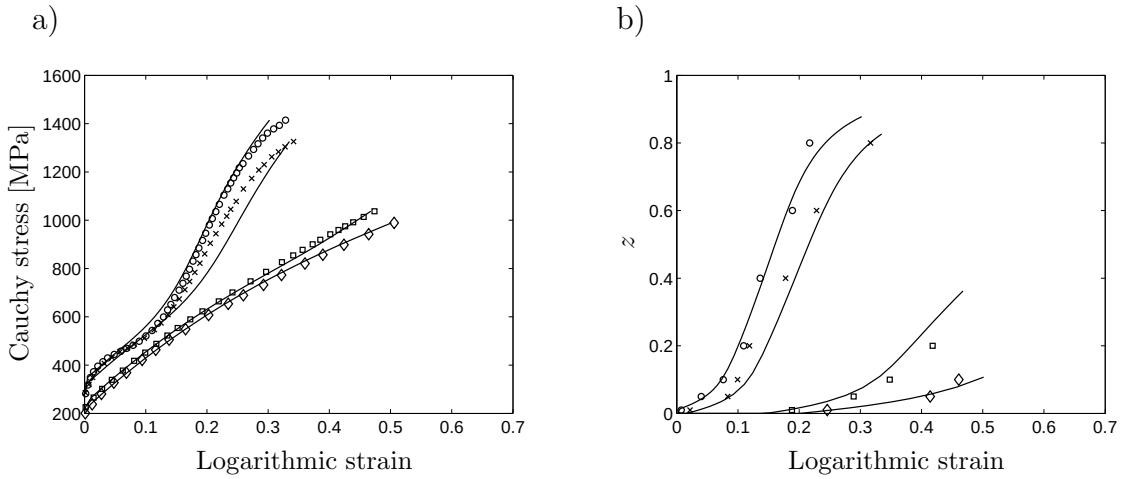

Figure 2: (a) Mechanical response in uniaxial tension. The experimental data is taken from Onyuna (2003). (b) The volume fraction of martensite as a function of the logarithmic strain. The initial temperatures are ○ – 213 K, × – 233 K, □ – 293 K and ◇ – 313 K.

temperature evolution due to dissipation from plastic deformation and due to heat released

during phase transformation will influence the progress of phase transformation and the mechanical response to a large extent. To be able to trace the effects of the temperature evolution, simulations of the material response in thermo-mechanically coupled uniaxial tensile tests were also conducted. The results are presented in Figs. 3 and 4. Fig. 3 also shows some experimental results from tensile testing of SUS304 stainless steel conducted at room temperature, taken from Talonen *et al.* (2005), verifying the magnitude of the simulated temperature increase. The simulations have different initial temperatures and thermo-mechanically coupled conditions are assumed. Compared to the isothermal analyses in Fig. 2, it can be clearly seen in Fig. 4b how the evolving temperature reduces the growth of a martensitic phase.

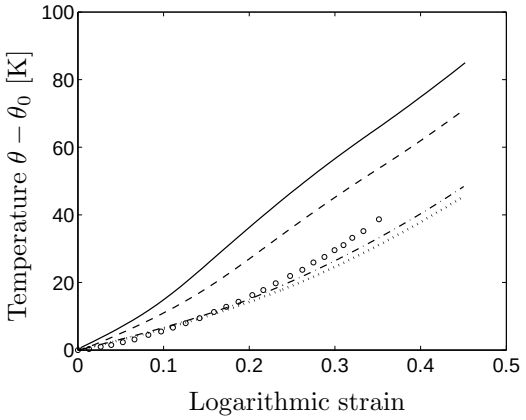

Figure 3: Temperature evolution in thermo-mechanically coupled simulations of uniaxial tensile tests at different initial temperatures. Thermo-mechanically coupled conditions are assumed. Solid line – 213 K, dashed line – 233 K, dash-dotted line – 293 K and dotted line – 313 K. The circles represent experimental data obtained at room temperature, taken from Talonen *et al.* (2005).

4.2 Forming limit diagram

The forming limit diagram (FLD) is a tool often encountered in relation to sheet metal forming. The diagram is used to predict the risk that a given strain state will trigger localized deformation, possibly leading to subsequent fracture or locally inadequate sheet thickness. The FLD can in this way be used to evaluate the formability of a certain material. Here, the forming limit diagrams are calculated for both isothermal and adiabatic conditions, using the present model. The FLD for a biaxially loaded plate is based on the formation of a shear band in the plate, cf. Fig. 5. To determine the onset of shear band formation, the method given by Marciniak and Kuczynski (1967) is used. To fulfill deformation compatibility and stress equilibrium along the edge of the shear band, the

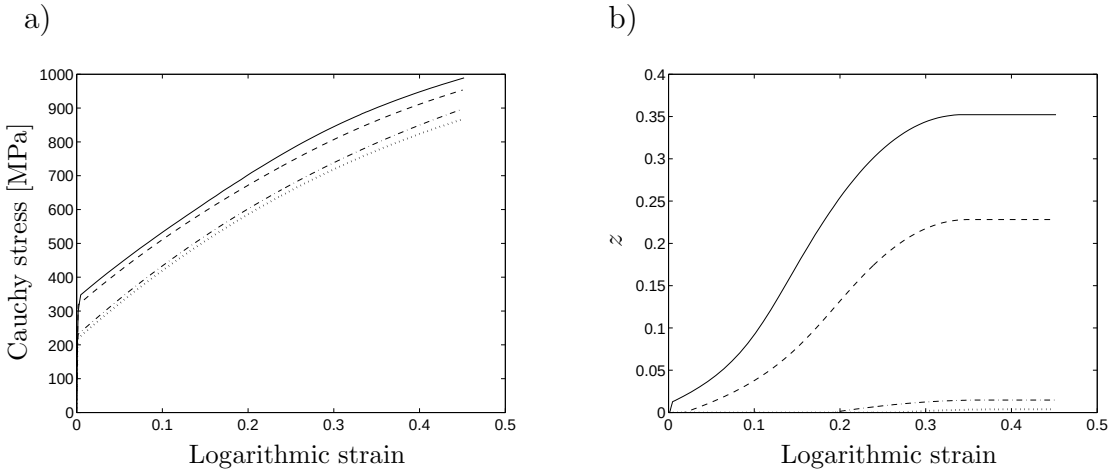

Figure 4: Results from thermo-mechanically coupled uniaxial tensile tests simulated at different initial temperatures. Thermo-mechanically coupled conditions are assumed. (a) Mechanical response. (b) Volume fraction of martensite. Solid lines – 213 K, dashed lines – 233 K, dash-dotted lines – 293 K and dotted lines – 313 K.

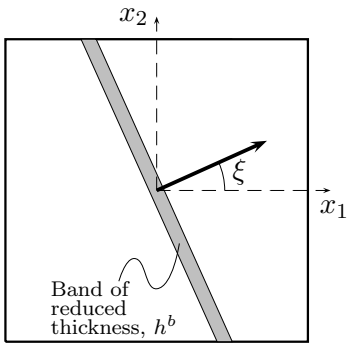

Figure 5: Illustration of quantities used in the FLD calculations. A plate of thickness h is loaded in the plane. The plate contains an initial inhomogeneity in the form of a band with reduced thickness h^b. This band is oriented an angle ξ from the principal axes x_1 and x_2 of the plate.

following relations must be fulfilled

$$F^b_{\alpha\beta} = F_{\alpha\beta} + d_\alpha m_\beta \tag{34}$$

and

$$m_\alpha P^{\mathrm{b}}_{\alpha\beta} h^{\mathrm{b}} = m_\alpha P_{\alpha\beta} h \tag{35}$$

Quantities inside the shear band are denoted by a superscript b. Plane stress is assumed and Greek indices are used to indicate that the relations above hold in the plane, i.e. the indices take on the values 1 and 2. The orientation of the shear band in the reference configuration is defined by $\boldsymbol{m} = [\cos(\xi) \ \sin(\xi)]$, where ξ is the angle of the shear band, cf. Fig. 5. The first Piola-Kirchhoff stress tensor is denoted by $\boldsymbol{P} = \boldsymbol{\tau}\boldsymbol{F}^{-T}$ while h and h^{b} are the thicknesses of the plate outside of, and inside, the shear band. The relation h^{b}/h is typically chosen in the range of 0.99 to 0.999. To obtain the FLD, the initiation of shear band formation is determined for a spectrum of different relations between the logarithmic strains in the 11 and 22 directions. In the algorithm for finding the initiation of the shear band, the material is proportionally loaded with a specific ratio between these strain components. In each load step, equation (35) is solved with the additional requirements set by (34). In the non-linear system of equations (35) that arise in each load step, everything is known except the first Piola-Kirchhoff stress tensor in the shear band, $P^{\mathrm{b}}_{\alpha\beta}$, which is given by the deformation gradient in the shear band, $F^{\mathrm{b}}_{\alpha\beta}$, and coherent internal variables. Thus, the unknown quantities to be solved for are d_α. The material is loaded until the ratio between the rate of effective plastic strain inside and outside of the shear band, respectively, exceeds a factor of 10. For a given relation between the logarithmic strains in the 11 and 22 directions, the angle ξ of the shear band is not known in advance. To find the correct angle, (35) is solved for a wide range of angles and the value of ξ that is the first to trigger localization is chosen as the direction of the shear band.

To be able to compare how the FLD changes under varying conditions, a study is performed based on four different initial temperatures; 213 K, 233 K, 293 K and 313 K. Each of these analyses are conducted under both adiabatic as well as isothermal conditions, where in the latter case, any heat generation is excluded. The results from these analyses are shown in Fig. 6 and Fig. 7. Together with the FLD:s, the fraction of martensite z, is shown by figures in the middle rows and the corresponding temperature rise is shown in the bottom row figures. The fractions of martensite and the temperature histories are taken from the final state, i.e. at the onset of shear band formation when the interruption criterion is met. In Figs. 6 and 7, the dash-dotted lines show the strain paths followed during the simulated deep-drawing process discussed below. The highest formability is found for the isothermal analysis with an initial temperature of 293 K. This may seem surprising since the hardening of the material, due to the high rate of phase transformation, is considerably more pronounced for the lower temperatures, cf. Fig. 2. This phenomenon is, however, related to the effect discussed in Hallberg *et al.* (2007), where the microstructural transformation into the stiffer martensite phase stabilizes the localization and thereby delays it. For the lower temperatures, nearly all transformation takes place well before any initialization of shear bands has occurred, while for the higher temperatures and especially at 293 K, transformation still takes place after the onset of localization. From Figs. 6 and 7, it is also obvious that this stabilizing effect is restricted by the internal heat genera-

tion. The temperature rise leads to a decrease both in the rate of phase transformation and also of the yield stress, giving thermal softening. The decrease in the rate of phase transformation is clearly seen in the middle row figures. It can be noted that the volume fraction of martensite as seen in the middle-row graphs of Figs. 6 and 7 correspond well to the uniaxial simulation results shown in Fig. 4b. Accordingly, the temperature levels in the bottom-row graphs of Figs. 6 and 7 reflect well the heat generation in the uniaxial case, cf. Fig. 3.

4.3 Deep-drawing process

A fully thermo-mechanically coupled cup deep-drawing process, as illustrated in Fig. 8, is considered. A metal sheet of initial thickness 1 mm and initial diameter 152 mm is used and the punch velocity is set to $v = 10$ mm/s. The geometrical parameters in Fig. 8 are set to d_1=60 mm, r_1=6 mm, d_2=65 mm and r_2=6 mm, respectively. A Coulomb friction coefficient of 0.1 is used at all contacting surfaces except between the punch and the plate where a value of 0.15 is used. The present model is implemented as a user subroutine in Abaqus Standard and is solved as a fully coupled system. The metal sheet is discretized using thermo-mechanically coupled four-node, bi-linear and axisymmetric elements of type CAX4T. The thickness of the sheet is discretized using 16 elements while 800 elements are used in the radial direction.

Fig. 9 shows the punch force versus punch displacement obtained from simulations, conducted at four different initial temperatures under isothermal as well as thermo-mechanically coupled conditions. As expected, the isothermal simulations allow more martensite to be formed since no temperature increase is present to reduce the extent of the phase transformation, cf. Figs. 10 and 11. The occurrence of martensite again helps in stabilizing the localization region of the material, thereby delaying the progression of localized deformation. Note that the strain paths followed in the localization region of the plate during the deep-drawing process are plotted with dash-dotted lines in the FLD-graphs in Figs. 6 and 7, showing a good agreement between the deep-drawing simulations and the FLD-calculations. Circles indicate the strain state at which localization is initiated in the cup material. These strain paths are obtained by using the logarithmic strains in the drawing direction and in the circumferential direction of the cup. As the direction of the localization is known, a simple criterion for detecting the onset of localization in the finite element simulations is used. This criterion is taken as the difference between the rates of the logarithmic strain in the drawing direction and in the circumferential direction being greater than 5.5. This value is chosen since it gives a good agreement between the isothermal FLD curves and the isothermal deep-drawing simulations. Initiation of localization by this criterion is shown by circles in the graphs of Fig. 9. It can be noted that the strain states at initiation of localized deformation for the thermo-mechanically coupled deep-drawing

simulations appear between the FLD-curves corresponding to adiabatic and isothermal conditions, respectively. This is to be expected since heat conduction will limit the temperature increase – as compared to the adiabatic situation – in the region of localized deformation and thereby allow some additional martensite to form and postpone further localization there. The exact locations of the localization points, as shown by circles in Figs. 6 and 7, are to some extent influenced by the chosen mesh discretization and also by the number of solution steps taken during the simulations. The precise strain state at initial localization is, however, expected to occur close to the strain states indicated.

The thermo-mechanically coupled simulations involve less martensite due to the substantial temperature increase. The effect of this reduced phase transformation is clearly seen in Fig. 9 where localization occurs much earlier in the thermo-mechanically coupled simulations as compared to the isothermal simulations. Comparing the graphs in Fig. 9 it can be noted that a maximum formability of the material is obtained for isothermal conditions at an initial temperature of 293 K, consistent with the conclusions drawn from the FLD calculations. Under thermo-mechanically coupled conditions, the most beneficial initial temperature for forming is less obvious. A maximum drawing-depth of 31.0 mm before localization – when considering heat generation – is obtained for an initial temperature of 313 K. This depth is, however, only slightly greater than the 30-30.3 mm achieved at the other three initial temperatures studied. The fact that the maximum drawing-depth, i.e. the maximum formability, is relatively unaffected by the initial temperature during the thermo-mechanically coupled simulations is reflected by the results in the FLD-graphs seen in Figs. 6 and 7. The FLD-lines corresponding to the adiabatic case lie at almost the same strain level, irrespective of the initial temperature.

The volume fractions of martensite under isothermal conditions are illustrated in Fig. 10 and for the thermo-mechanically coupled case in Fig. 11. The temperature increase obtained from the thermo-mechanically coupled simulations are shown in Fig. 12. The last deformation state shown in each of these figures correspond to the localization criterion described previously, i.e. the same states as are shown by circles in Figs. 6, 7 and 9. The deep-drawing results presented in Figs. 10, 11 and 12 further illustrates the influence of interacting phase transformation and heat generation on the formability of the sheet material. The maximum formability obtained for a temperature of 293 K and under isothermal conditions is clearly shown in Fig. 10c. Correspondingly, the situation at thermo-mechanically coupled conditions where no clearly distinguishable temperature for maximum formability can be found, is shown by the illustrations in Fig. 11. Comparing Figs. 11 and 12, a substantial heat generation can be noted in the localization region, reducing the progression of phase transformation and thereby also reducing the stabilizing effect of martensite formation on the localization region. Note that the temperature increase at the onset of localization in the thermo-mechanically coupled deep-drawing simulations is higher than that found in the FLD diagrams in Figs. 6 and 7. The reason for this is that localization

occur at a later state – i.e. at larger strains – in the thermo-mechanically coupled case, allowing more heat to be generated. The strong influence of temperature on the phase transformation and thereby also on the formability of the sheet can be utilized in practical applications for obtaining optimal formability. This can be achieved by controlling the temperature distribution in the forming tools, allowing some control over the martensite distribution in the final product. This is, however, not reflected in the present simulations since no heat conduction between the plate and the tools is included.

5 Concluding remarks

A constitutive model of thermo-mechanically coupled finite strain plasticity influenced by martensitic phase transformation is presented. The model is formulated within a thermodynamic framework, giving a physically sound format where the thermodynamic forces, driving the phase transformation based on a lowering of the Gibbs energy, are conveniently identifiable. The model is calibrated against a common Ni-Cr steel of AISI304-type, allowing illustrative simulations to be performed. It becomes clear that the thermal effects considered in the present formulation have much impact on the material behavior. This is seen, not least, in the impact found on forming limit diagrams, an important engineering tool in sheet metal forming and considered in the present work.

References

Berveiller, M. and Fischer, F. D., editors (1997). *Mechanics of Solids with Phase Changes*. Number 368 in CISM Courses and Lectures. Springer Wien New York.

Christ, D. and Reese, S. (2009). A finite element model for shape memory alloys considering thermomechanical couplings at large strains. *International Journal of Solids and Structures*, **46**, 3694–3709.

Coleman, B. D. and Gurtin, M. E. (1967). Thermodynamics with internal state variables. *Journal of Chemical Physics*, **47**, 597–613.

Fischer, F. D. (1990). A micromechanical model for transformation plasticity in steels. *Acta Metallurgica et Materialia*, **38**(8), 1535–1546.

Fischer, F. D., Berveiller, M., Tanaka, K., and Oberaigner, E. R. (1994). Continuum mechanical aspects of phase transformations in solids. *Archive of Applied Mechanics*, **64**, 54–85.

Fischer, F. D., Oberaigner, E. R., Tanaka, K., and Nishimura, F. (1998). Transformation induced plasticity, revised and updated formulation. *International Journal of Solids and Structures*, **35**, 2209–2227.

Fischer, F. D., Reisner, G., Werner, E., Tanaka, K., Cailletaud, G., and Antretter, T. (2000). A new view on transformation induced plasticity (TRIP). *International Journal of Plasticity*, **16**, 723–748.

Fu, S., Huo, Y., and Müller, I. (1993). Thermodynamics of pseudoelasticity - an analytical approach. *Acta Mechanica*, **99**, 1–19.

Ganghoffer, J. F. and Simonsson, K. (1998). A micromechanical model of the martensitic transformation. *Mechanics of Materials*, **27**, 125–144.

Geijselaers, H. J. M. and Perdahcioglu, E. S. (2009). Mechanically induced martensitic transformation as a stress-driven process. *Journal of the Iron and Steel Institute*, **60**, 29–31.

Greenwood, G. W. and Johnson, R. H. (1965). The deformation of metals under small stresses during phase transformations. *Physica Status Solidi*, **283 A**, 403–422.

Håkansson, P., Wallin, M., and Ristinmaa, M. (2005). Comparison of isotropic hardening and kinematic hardening in thermoplasticity. *International Journal of Plasticity*, **7**, 1435–1460.

Hallberg, H., Håkansson, P., and Ristinmaa, M. (2007). A constitutive model for the formation of martensite in austenitic steels under large strain plasticity. *International Journal of Plasticity*, **23**(7), 1213–1239.

Kröner, E. (1959). Allgemeine Kontinuumstheorie der Versetzungen und Eigenspannungen. *Archive for Rational Mechanics and Analysis*, **4**(1), 273–334.

Leblond, J. B., Mottet, G., and Devaux, J. C. (1986a). A theoretical and numerical approach to the plastic behaviour of steels during phase transformations - I. derivation of general relations. *Journal of the Mechanics and Physics of Solids*, **34**(4), 395–409.

Leblond, J. B., Mottet, G., and Devaux, J. C. (1986b). A theoretical and numerical approach to the plastic behaviour of steels during phase transformations - II. study of classical plasticity for ideal-plastic phases. *Journal of the Mechanics and Physics of Solids*, **34**(4), 411–432.

Lee, E. H. and Liu, D. T. (1967). Finite strain plasticity particularly for plane waves. *Journal of Applied Physics*, **38**, 19–27.

Lee, M.-G., Kim, S.-J., Han, H. N., and Jeong, W. C. (2009). Implicit finite element formulations for multi-phase transformation in high carbon steel. *International Journal of Plasticity*, **25**, 1726–1758.

Levitas, V. (1998). Thermomechanical theory of martensitic phase transformation in inelastic materials. *International Journal of Solids and Structures*, **35**, 889–940.

Levitas, V., Idesman, A. V., Olson, G. B., and Stein, E. (2002). Numerical modelling of martensitic growth in a elastoplastic material. *Philosophical Magazine A*, **82**(3), 429–462.

Levitas, V. I., Idesman, A. V., and Olson, G. B. (1998). Continuum modeling of strain-induced martensitic transformation at shear-band intersections. *Acta Materialia*, **47**(1), 219–233.

Ludwigson, D. C. and Berger, J. A. (1969). Plastic behaviour of metastable austenitic stainless steels. *Journal of the Iron and Steel Institute*, pages 63–69.

Magee, C. L. (1969). The nucleation of martensite. *ASM International, Materials Park*, pages 115–155.

Mahnken, R., Schneidt, A., and Antretter, T. (2009). Macro modelling and homogenization for transformation induced plasticity of a low-alloy steel. *International Journal of Plasticity*, **25**, 183–204.

Marciniak, Z. and Kuczynski, K. (1967). Limit strains in the process of stretch-forming sheet metal. *International Journal of Mechanical Sciences*, **9**, 609–620.

Mohr, D. and Jacquemin, J. (2008). Large deformation of anisotropic austenitic stainless steel sheetsat room temperature: Multi-axial experiments and phenomenological modeling. *Journal of the Mechanics and Physics of Solids*, **56**, 2935–2956.

Olson, G. B. and Cohen, M. (1972). A mechanism for the strain-induced nucleation of martensitic transformations. *Journal of the Less-Common Metals*, **28**, 107–118.

Olson, G. B. and Cohen, M. (1975). Kinetics of strain-induced martensitic nucleation. *Metallurgical Transactions*, **6A**, 791–795.

Onyuna, M. O. (2003). *Deformation behaviour and martensitic transformations in metastable austenitic steels and low alloyed multiphase steels*. Ph.D. thesis, Department of Materials Science and Technology, Freiberg University of Mining and Technology.

Petit-Grostabussiat, S., Taleb, L., and Jullien, J.-F. (2004). Experimental results on classical plasticity of steels subjected to structural transformations. *International Journal of Plasticity*, **20**(8-9), 1371–1386.

Ramirez, J. A. C., Tsuta, T., Mitani, Y., and Osakada, K. (1992). Flow Stress and Phase Transformation Analyses in the Austenitic Stainless Steel under Cold Working. Part 1,

phase transformation characteristics and constitutive formulation by energetic criterion. *Japanese Society of Mechanical Engineering*, **35**(2), 201–209.

Rengarajan, G., Kumar, R. K., and Reddy, J. N. (1998). Numerical modeling of stress induced martensitic phase transformations in shape memory alloys. *International Journal of Solids and Structures*, **35**(14), 1489–1513.

Ristinmaa, M., Wallin, M., and Ottosen, N. S. (2007). Thermodynamic format and heat generation of isotropic hardening plasticity. *Acta Mechanica*, **194**(1), 103–121.

Silva, E. P., Pacheco, P. M. C. L., and Savi, M. A. (2004). On the thermo-mechanical coupling in austenite-martensite phase transformation related to the quenching process. *International Journal of Solids and Structures*, **41**, 1139–1155.

Stringfellow, R. G., Parks, D. M., and Olson, G. B. (1992). A constitutive model for transformation plasticity accompanying strain-induced martensitic transformation in metastable austenitic steels. *Acta Metallurgica et Materialia*, **40**(7), 1703–1716.

Talonen, J., Nenonen, P., Pape, G., and Hänninen, H. (2005). Effect of strain rate on the strain-induced martensite transformation and mechanical properties of austenitic stainless steels. *Metallurgical and Materials Transactions*, **36**(2), 421–432.

Turteltaub, S. and Suiker, A. S. J. (2005). A multiscale thermomechanical model for cubic to tetragonal martensitic phase transformations. *International Journal of Solids and Structures*, **43**, 4509–4545.

Wolff, M., Böhm, M., and Helm, D. (2008). Material behavior of steel - Modeling of complex phenomena and thermodynamic consistency. *International Journal of Plasticity*, **24**, 746–774.

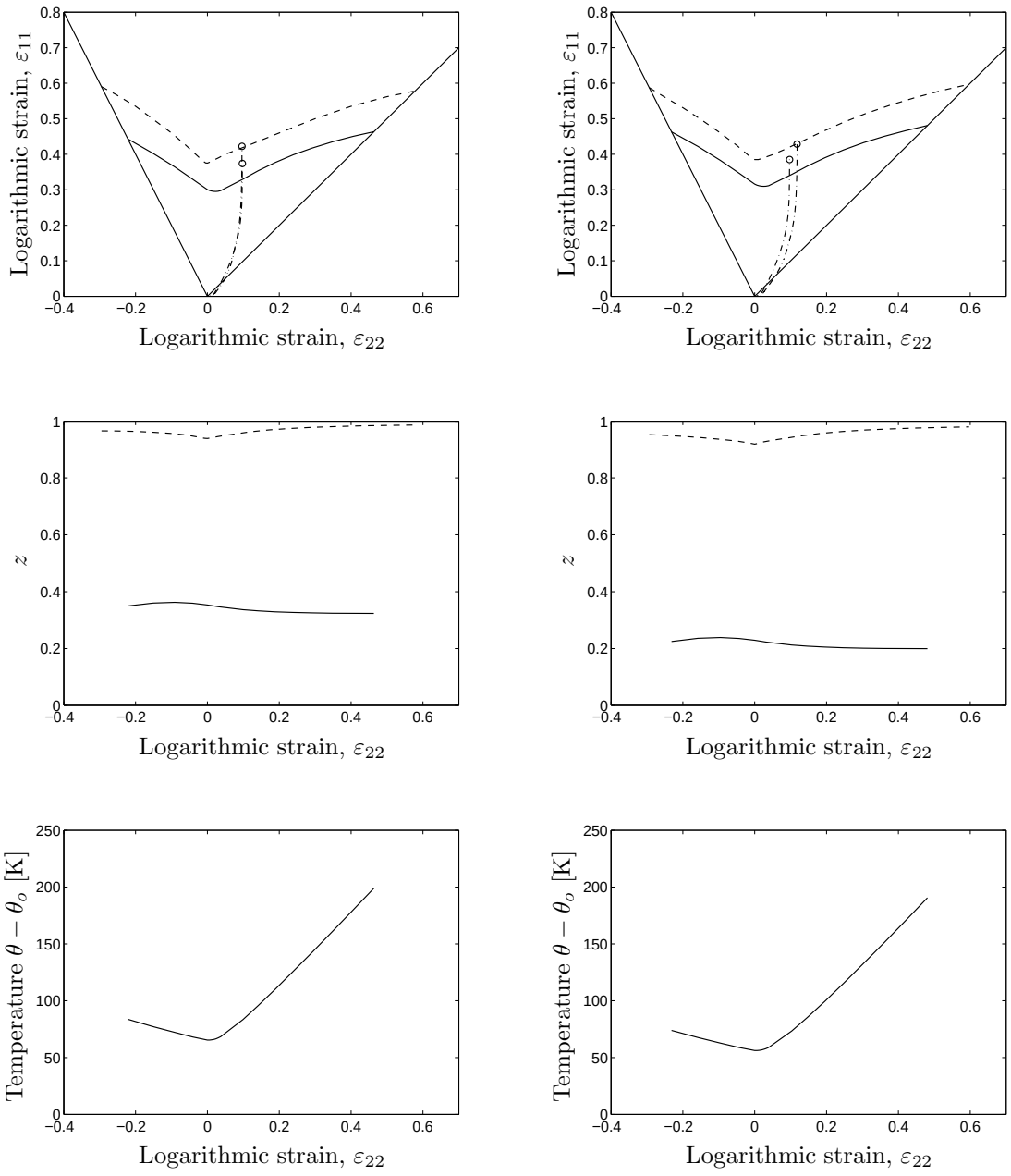

Figure 6: The left and right columns represents analyses with an initial temperature of 213 K and 233 K, respectively. The figures in the top row are the forming limit diagrams. The figures in the middle row shows the fraction of martensite at the onset of shear band formation and the bottom row figures show the temperature change at shear band initiation. Solid lines represent results from adiabatic simulations and dashed lines correspond to isothermal simulations. Similar results for the initial temperatures 293 K and 313 K are shown in Fig. 7. Dash-dotted lines show the strain paths traced in the localization region of the plate during the simulations of cup deep-drawing processes, also considered in the present work.

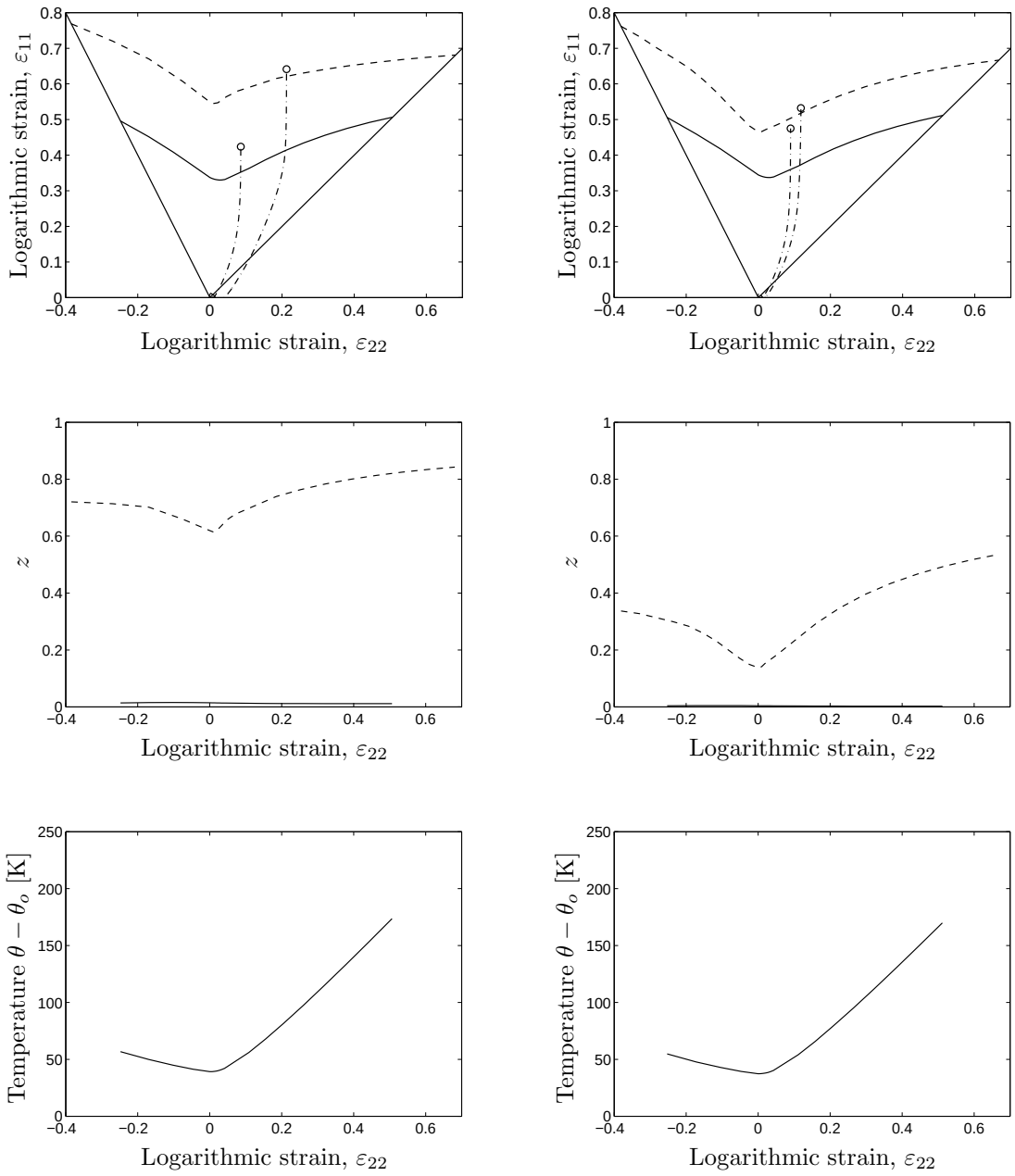

Figure 7: Fig. 6 continued. The left and right columns represents analysis with an initial temperature of 293 K and 313 K, respectively.

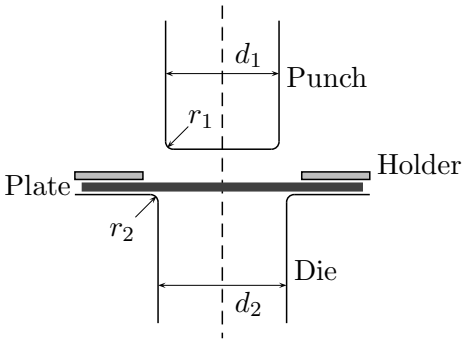

Figure 8: Geometry of the deep-drawing setup.

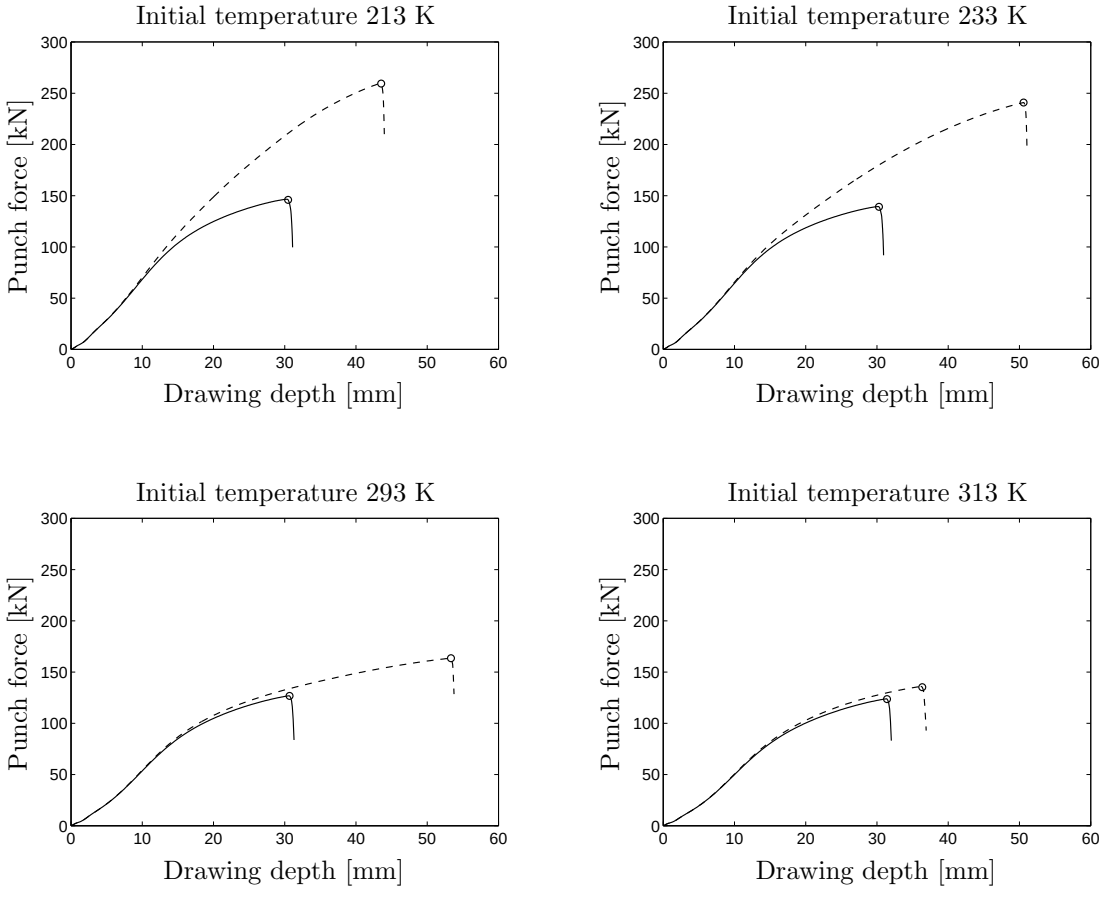

Figure 9: Punch force versus drawing depth at four different initial temperatures. Solid lines show results from thermo-mechanically coupled simulations and dashed lines represent results from isothermal simulations. Circles show the point where localized deformation is initiated.

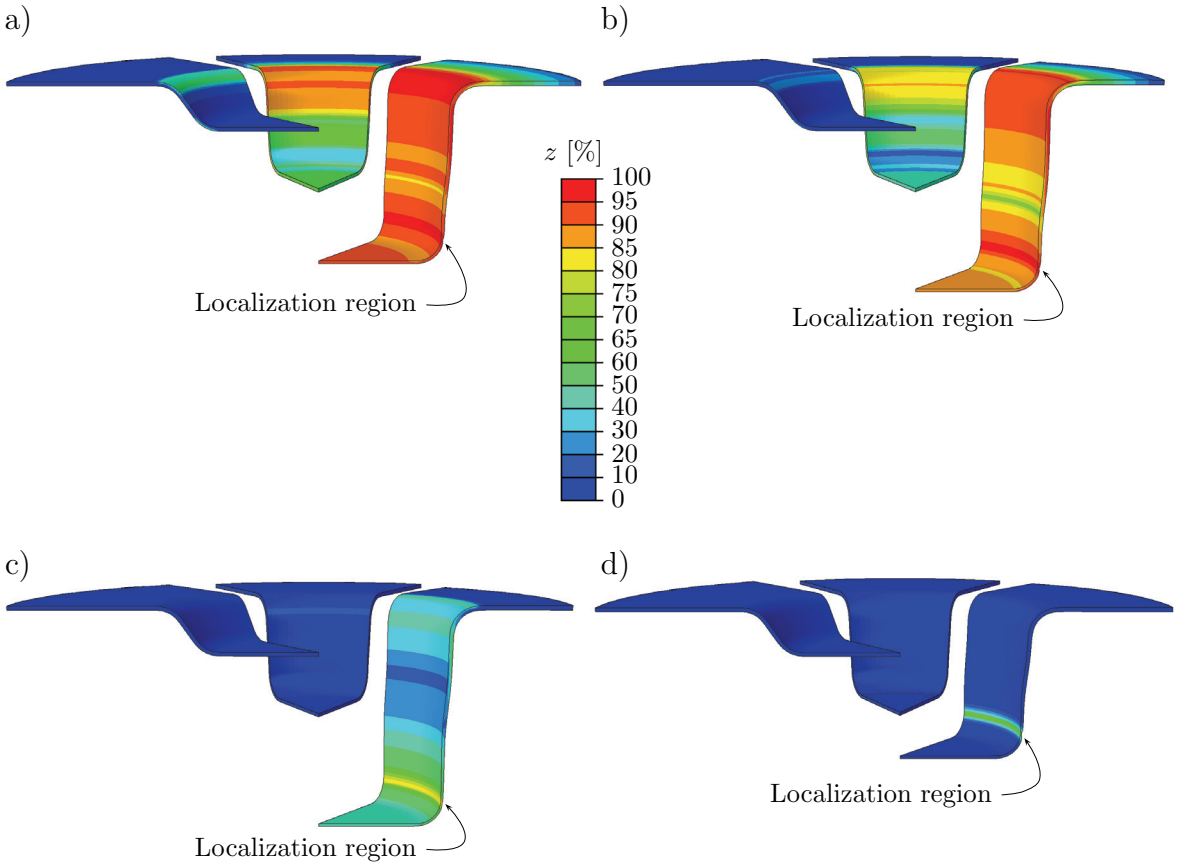

Figure 10: Results from isothermal deep-drawing simulations showing the volume fraction of martensite in the material. (a) Temperature 213 K, drawing-depths 10.0, 25.0 and 43.0 mm. (b) Temperature 233 K, drawing-depths 10.0, 25.0 and 50.1 mm. (c) Temperature 293 K, drawing-depths 10.0, 25.0 and 52.6 mm. (d) Temperature 313 K, drawing-depths 10.0, 25.0 and 36.0 mm.

DOI: 10.1016/j.ijsolstr.2010.02.019

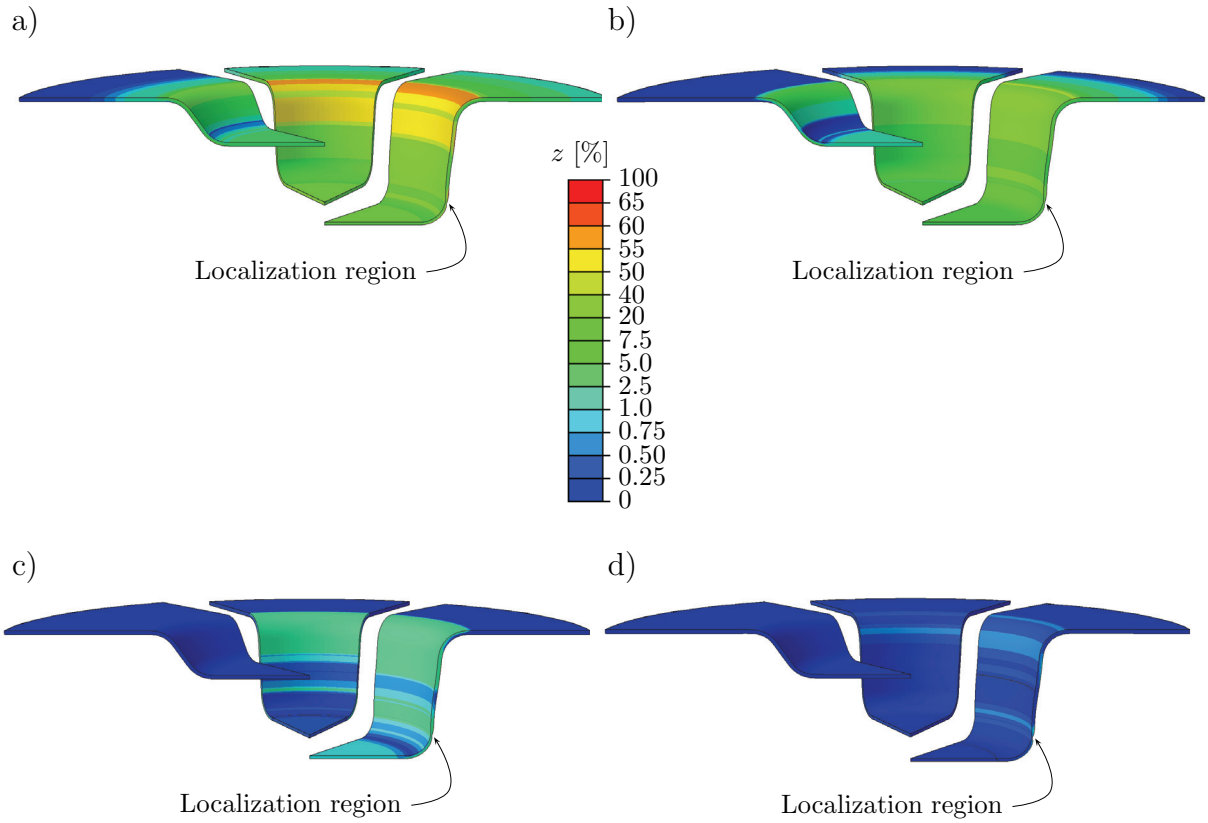

Figure 11: Results from thermo-mechanically coupled deep-drawing simulations showing the volume fraction of martensite in the material. (a) Initial temperature 213 K, drawing-depths 10.0, 25.0 and 30.3 mm. (b) Initial temperature 233 K, drawing-depths 10.0, 25.0 and 30.0 mm. (c) Initial temperature 293 K, drawing-depths 10.0, 25.0 and 30.3 mm. (d) Initial temperature 313 K, drawing-depths 10.0, 25.0 and 31.0 mm.

DOI: 10.1016/j.ijsolstr.2010.02.019

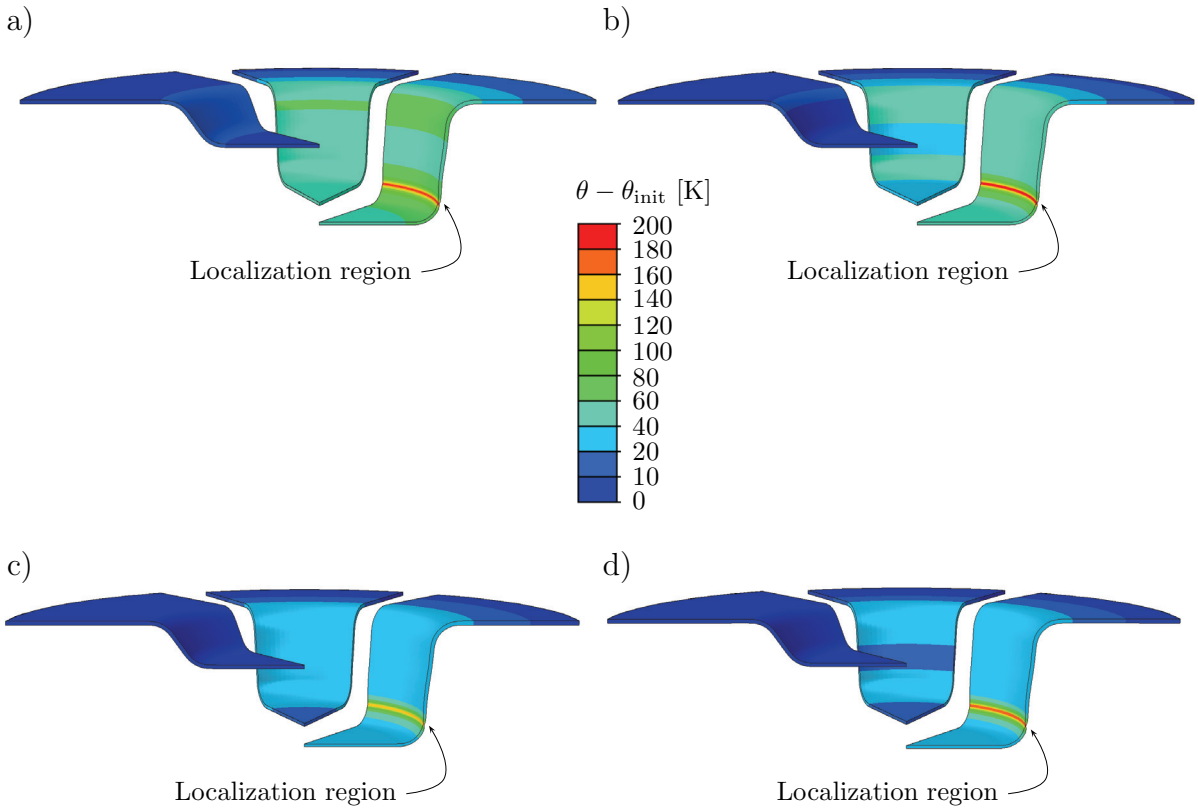

Figure 12: Results from thermo-mechanically coupled deep-drawing simulations showing the temperature increase in the material. (a) Initial temperature 213 K, drawing-depths 10.0, 25.0 and 30.3 mm. (b) Initial temperature 233 K, drawing-depths 10.0, 25.0 and 30.0 mm. (c) Initial temperature 293 K, drawing-depths 10.0, 25.0 and 30.3 mm. (d) Initial temperature 313 K, drawing-depths 10.0, 25.0 and 31.0 mm.

DOI: 10.1016/j.ijsolstr.2010.02.019